Integration of Weather Research and Forecasting (WRF) Model with Regional Coastal Ecosystem Model to Simulate the Hypoxic Conditions

7 authors, including:

Muhammad Ali Hafeez
Port and Airport Research Institute
8 PUBLICATIONS   **17** CITATIONS

SEE PROFILE

Yoshiyuki Nakamura
Yokohama National University
142 PUBLICATIONS   **809** CITATIONS

SEE PROFILE

Takayuki Suzuki
Yokohama National University
129 PUBLICATIONS   **425** CITATIONS

SEE PROFILE

Tetsunori Inoue
Port and Airport Research Institute
69 PUBLICATIONS   **416** CITATIONS

SEE PROFILE

Some of the authors of this publication are also working on these related projects:

Project   Special Issue "Advances on Remote Sensing of Precipitation " (Atmosphere) View project

Project   Water exchange and circulation in processes in coastal brackish lakes. View project

Integration of Weather Research and Forecasting (WRF) model with regional coastal ecosystem model to simulate the hypoxic conditions

Muhammad Ali Hafeez [a,*], Yoshiyuki Nakamura [b], Takayuki Suzuki [b], Tetsunori Inoue [c], Yoshitaka Matsuzaki [c], Kangnian Wang [d], Abdul Moiz [e]

[a] Graduate School of Urban Innovation, Yokohama National University, Tokiwadai 79-5, Hodogaya, Yokohama 240-8501, Japan
[b] Faculty of Urban Innovation, Yokohama National University, Tokiwadai 79-5, Hodogaya, Yokohama 240-8501, Japan
[c] Marine Environmental Information Group, Port and Airport Research Institute, Nagase 3-1-1, Yokosuka, Kanagawa 239–0826, Japan
[d] Department of Socio-Cultural Environmental Studies, Graduate School of Frontier Sciences, The University of Tokyo, Kashiwanoha 5-1-5, Chiba 277-8563, Japan
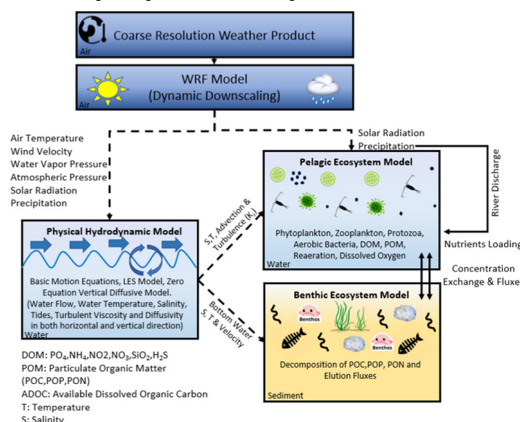[e] Department of Civil Engineering, The University of Tokyo, Hongo 7-3-1, Bunkyo-Ku, Tokyo 113-8656, Japan

HIGHLIGHTS

- Integration of WRF with 3D hydrodynamic and coastal ecosystem model is presented.
- Downscaling of coarse weather product by WRF to drive 3D coastal ecosystem model.
- Accurate simulations of physical and biogeochemical processes were conducted.
- Bottom dissolved oxygen in shallow and deep water was well reproduced.
- Hypoxic events were also calculated from simulated dissolved oxygen.

GRAPHICAL ABSTRACT

Integrated modelling framework showing the coupled model compartments with the respective flow of input variables from weather model to hydrodynamic and ecosystem model.

ARTICLE INFO

ABSTRACT

Regional ocean models require accurate weather data for atmospheric boundary conditions such as air temperature, wind speed, and direction to simulate the coastal environment. In this study, a numerical modelling framework was developed to simulate different physical, chemical, and biological processes in a semi-enclosed coastal ecosystem by integrating the Weather Research and Forecasting (WRF) model with a 3D hydrodynamic and ecosystem model (Ise Bay Simulator). The final analytic data of the global forecast system released by the National Centers for Environmental Prediction with a 0.25° horizontal resolution was used as an atmospheric boundary condition for the WRF model to dynamically downscale the weather information to a spatial and temporal fine resolution. This modelling framework proved to be an effective tool to simulate the physical and biogeochemical processes in a semi-enclosed coastal embayment. The WRF-driven ecosystem simulation and recorded Automated Meteorological Data Acquisition System (AMeDAS)-driven ecosystem simulation results were further compared with the observed data. The performance of both the recorded AMeDAS and WRF generated weather datasets were equally good, and more than 80% of the variation in bottom dissolved oxygen for shallow water and more than 90% for deep water was reproduced.

© 2021 Elsevier B.V. All rights reserved.

* Corresponding author.
E-mail addresses: hafeez-ali-ry@ynu.jp, Engrali.uet@gmail.com (M.A. Hafeez).

1. Introduction

Hypoxia is a significant issue affecting aquatic habitats, such as open oceans and coastal areas worldwide (Carstensen et al., 2014; Matear and Hirst, 2003; Song et al., 2020). The depletion of oxygen can greatly affect the biodiversity of the ocean (Vaquer-Sunyer and Duarte, 2008) and community structures and can alter the functioning of the ecosystem (Rabalais et al., 2002). The hypoxic water mass not only causes mortality in aquatic species directly but also limits the availability of appropriate habitats (Stramma et al., 2008). The conditions in the sediments at the bottom of the ocean further deteriorate when the dissolved oxygen level remains low for a protracted period (Keister et al., 2000). Therefore, hypoxic and anoxic water masses have potentially adverse impacts on ecosystem functioning (Diaz and Rosenberg, 2008), fisheries industries associated with the ocean (Rheuban et al., 2018), and the dynamics of inorganic and organic matter (Galgani et al., 2014).

Ise Bay is a semi-enclosed water body with characteristics of summer season hypoxia that is typically observed in eutrophic enclosed bays. Its topography and water exchange characteristics play an important role in the occurrence of hypoxic water mass (Fujiwara et al., 2002; Nakao and Matsuzaki, 1995). Whenever oxygen consumption by the decomposition of organic matter by bacteria (biochemical processes) exceeds oxygen supply (physical processes), the bottom water becomes hypoxic (Kasai, 2014; Katin et al., 2019; Officer et al., 1984). The physical processes, especially the water exchange at the bay mouth, follow a seasonal pattern and show a significant decline in the intrusion of oxygen-rich oceanic water during the summer season (Hafeez et al., 2020; Kasai et al., 2004). In the summer season, the inner bay bottom water often gets separated from the surface and surrounding water, forming an older water pool with restricted oxygen supply (Hafeez et al., 2019; Tanaka and Ikeda, 2015).

The large-scale hypoxic water results in mass fish kill every year (Harada, 2008). The biomass of mega benthos and the richness of the main mega benthos species severely decrease during the summer season when hypoxic water mass develops (Hossain and Sekiguchi, 1996). As far as hypoxia development is concerned, seasonal variations in the spatial distributions of leading species, population structure, and their growth exhibit changes (Narita et al., 2003, 2006).

Identification of underlying causes is essential to mitigate the hypoxic environment. Simulation of different physical, chemical, and biological processes in a coastal ecosystem is vital for understanding the current system behaviour, future prediction, and its utilisation as a tool for an efficient and effective management system. Many effective numerical models have been proposed to simulate the coastal ecosystem (Blumberg and Mellor, 1987; Shchepetkin and McWilliams, 2005; Warren and Bach, 1992).

Regional ocean numerical simulation models require marine meteorological data as a crucial input for simulating the ecosystem environment because of its direct relationship with many environmental processes. For example, sea surface wind has a direct relationship with upwelling and downwelling (Galán et al., 2020; Rana et al., 2019), which may eventually lead to environmental problems. Similarly, air temperature affects water temperature and plays an important role in the development of water column stratification and eutrophication (Burt et al., 2012; Gamperl et al., 2020). Meteorological observations are generally concentrated in drylands with gauge density and spatial coverage, which is sufficient for the target area of interest. Field observations in the sea are made by mariners, monitoring buoys, ships, and satellites. Marine weather observations are of great importance as the number of observation stations in the sea are meager as compared to the observation stations on land, (Yelland et al., 1998). In the case of Ise Bay, several authors utilised the Automated Meteorological Data Acquisition System (hereafter AMeDAS) data to simulate the coastal ecosystem (Tanaka et al., 2014; Tanaka and Ikeda, 2015). The Japan Meteorological Agency (JMA) collects this data over 1300 rain gauges at an average interval of 17 km nationwide, and only 12 AMeDAS weather stations are available to create atmospheric boundary conditions for hydrodynamic and ecosystem simulations.

The mesoscale numerical weather model can produce high-resolution weather fields. Weather Research and Forecasting (WRF) model is famous for the downscaling of global weather products for local impact studies (Tang et al., 2016). However, there is a paucity of studies focusing on its integration with hydrodynamic and coastal ecosystem models to simulate water quality. The WRF model simulations greatly depend on lateral boundary conditions (hereafter LBC), land use data, and physical parameterisations. In the past, the WRF model was utilised to simulate meteorological parameters over Japan by using National Centers for Environmental Prediction final (NCEP-FNL) data (Matsuzaki et al., 2020; Minamiguchi et al., 2018). Different physical parameterisations were utilised, including the Yonsei University scheme for the planetary boundary layer (hereafter PBL), and submodels such as the Noah land surface model, Dudhia scheme for shortwave radiation, and the Rapid Radiative Transfer Model (hereafter RRTM) for longwave radiation. The results showed fair reproducibility of meteorological parameters (Minamiguchi et al., 2018). Other studies also showed reasonable simulations by using the aforementioned physical parameterisations (Shimadera et al., 2015a), but also discussed the uncertainties in the summertime precipitation (Shimadera et al., 2015b). Many researchers have also tried to assess the sensitivity of topography and land use data to substantiate their effectiveness (De Meij and Vinuesa, 2014; Jiménez-Esteve et al., 2018). As WRF simulations are sensitive to different datasets and parameterisation configurations, it is essential to obtain optimal configurations for the target research site "Ise Bay" by testing the best available input LBC and model settings. Therefore, in the first phase of this study, the weather simulations were conducted to obtain the optimum settings of the WRF model and input datasets. Furthermore, the WRF generated dataset was utilised to drive a 3D hydrodynamic and ecosystem model to simulate the bottom dissolved oxygen (hereafter DO).

The objective of this study is to develop an integrated modelling framework that can couple high-resolution downscaled weather data with a 3D hydrodynamic and ecosystem model. A 3D hydrodynamic and ecosystem model (Ise Bay Simulator) was modified and utilised to simulate different physical, chemical, and biological processes. This methodology can be used for study sites that are not easily evaluated owing to the scarcity of observed meteorological data. To assess the accuracy of this modelling framework, the hydrodynamic simulations and ecosystem simulations driven by both datasets (AMeDAS and WRF) were compared with the observed buoy data. The final analytic data of the global forecast system released by the National Centers for Environmental Prediction (NCEP-FNL) with a 0.25° horizontal resolution ('NCEP GDAS/FNL 0.25 Degree, DOI:10.5065/D65Q4T4Z,' n.d.), was used as the atmospheric boundary condition with the optimal WRF model settings to dynamically downscale the weather information on finer spatial and temporal resolutions.

2. Materials and methods

2.1. Study area

Ise Bay is located near the centre of Japan facing the Pacific Ocean, between latitudes 34.20° N and 35.40° N and longitudes 136.40° E and 137.40° E (Fig. 1). The bay has a large surface area of 1738 km^2 with a water volume of 33.9 km^3. It is connected to the Pacific Ocean through a mouth of 20 km length confined between several small islands, which is the only source of seawater exchange. Such topographic conditions make it a typical semi-enclosed water body with a higher enclosure index. The region surrounding Ise Bay can be roughly divided into ten major river systems. The widest and most populous one is the Kiso River system with a 9100 km^2 basin area and a 3.36 million population. The mean annual age of fresh river and seawater in the bay was
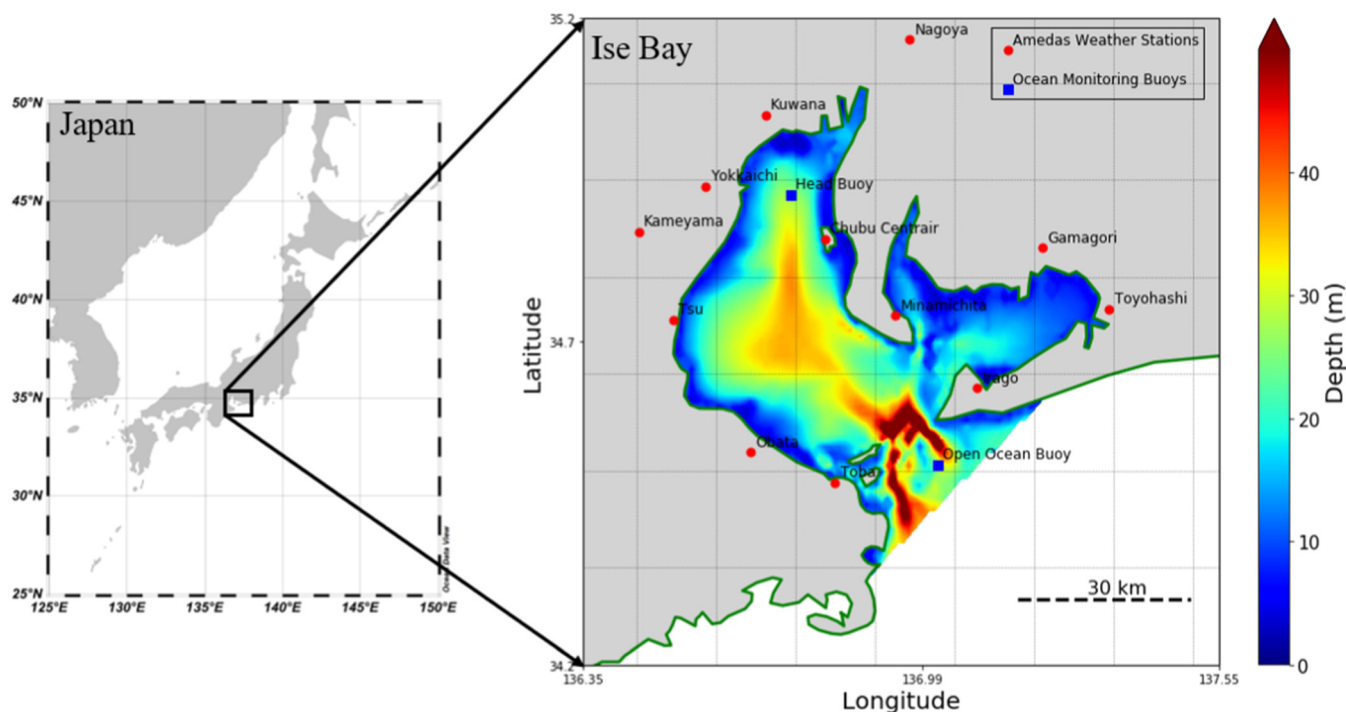
Fig. 1. Bathymetric map of Ise Bay and locations of monitoring stations. Solid red circles represent weather observation stations where hourly observations of air temperature, wind velocity, and precipitation are recorded by the JMA. Solid blue squares represent ocean monitoring buoys where in situ measurement of water quality in three layers; surface, middle, and bottom are made on an hourly basis by the Ministry of Land, Infrastructure, Transport, and Tourism (MLIT).

calculated to be 36.5 and 40.7 days, respectively (Tanaka and Ikeda, 2015). The bay has a larger surface area than other notable semi-enclosed bays in Japan, such as Osaka and Tokyo Bay. However, it has a relatively shallower average water depth of approximately 19.50 m and a maximum of 30 m depth towards the centre of the basin, which makes its bathymetry bowl-shaped. The bottom sediments in the northern and central part of the bay are silty clay, while southern and southwestern parts are sand, muddy sand, and sandy gravel (Ganmanee et al., 2003).

The water in the bay is rich in nutrients and highly turbid due to freshwater discharge along with sewage effluent from cities situated along the western and northern coasts of the bay. Recent progress of eutrophication in the bay brings red tides during the summer every year (Suzuki, 2016), followed by oxygen-poor water, which is abundant primarily in the central to western parts of the bay.

2.2. WRF model configuration

In this study, the WRF-ARW version 4.0 (Skamarock et al., 2019) was configured with two domains at 27 km and 9 km horizontal resolutions, respectively (Fig. 2). The model's vertical resolution was discretised with 40 full terrain-following σ levels with the model top at 10 hPa for both domains. There are 40 grid points in the east-west and north-south directions for Domain 01, and 46 grid points in both directions for Domain 02, which is the inner domain.

The physical parameterisation schemes used in both model domains include RRTM for shortwave and longwave radiation (Mlawer et al., 1997). This is one of the most accurate models developed specifically to address the atmospheric radiation measurement objective to further improve the radiation models in global climate models (GCMs) (Iacono et al., 2001). The Thompson Graupel scheme with six classes of moisture species was used as a microphysics scheme (Thompson et al., 2004). Noah land surface model scheme covering the soil temperature and moisture in four layers was used for land surface processes (Chen and Dudhia, 2001). For the PBL schemes, two combinations of PBL and surface layer schemes were tested, as, in the WRF model, fewer PBL

schemes can be used with particular surface layer schemes (Skamarock et al., 2019). Firstly a combination of Yonsei University PBL scheme (YSU) (Hong, 2010; Hong et al., 2006) with the Monin-Obukhov Similarity surface layer scheme (MOS) (Jiménez et al., 2012; Monin and Obukhov, 1959) was tested, and secondly, the Mellor-Yamada-Janjic (Eta) TKE PBL scheme (MYJ) (Mellor and Yamada, 1982) along with Monin-Obukhov (Janjic Eta) Similarity surface layer scheme (EMOS) (Chen et al., 1997; Janjic, 1990) was tested to obtain the most suitable combination for the subject research site. A Grell 3D cumulus scheme (Grell and Freitas, 2013) was applied to both domains for cumulus parameterisation.

The default United States Geological Survey (USGS) land use data, which comes with the WRF model, was used and obtained from the Global Land Cover Characteristics (GLCC) database (Loveland et al., 2000). In addition to USGS land use data having a coarse resolution, a high-resolution land-use geospatial authority of Japan (GSI) data with a relatively realistic land use category was also evaluated (Sashiyama and Yamamoto, 2014). The National Centers for Environmental Prediction (NCEP) Global Forecast System (GFS) Final (FNL) operational global analyses of 1° resolution ('NCEP FNL 1 Degree, DOI:10.5065/D6M043C6,' n.d.) and Global Data Assimilation System (GDAS) product of 0.25° ('NCEP GDAS/FNL 0.25 Degree, DOI:10.5065/D65Q4T4Z,' n.d.) were used for initial conditions with ingestion every 6 h.

The model was initialised at 0000 UTC 1 December 2015 and continuously integrated until 0000 UTC 31 December 2016. December 2015 was considered as the model spin-up and excluded from further comparisons with observation as well as ingestion to the ecosystem model. Table 1 summarises the entire model configuration and other input datasets evaluated in this study.

Table 2 summarises the cases tested to obtain the most suitable datasets as well as the WRF schemes to simulate weather conditions for Ise Bay. For case 1, the coarse 1° GFS LBC data was used with the first combination of the YSU and MOS scheme. The four-dimensional data assimilation (hereafter FDDA) was disabled for case 1. Subsequently, for case 2, the FDDA was enabled while keeping the same combination of schemes as in case 1. In case 3, the GSI land use data was
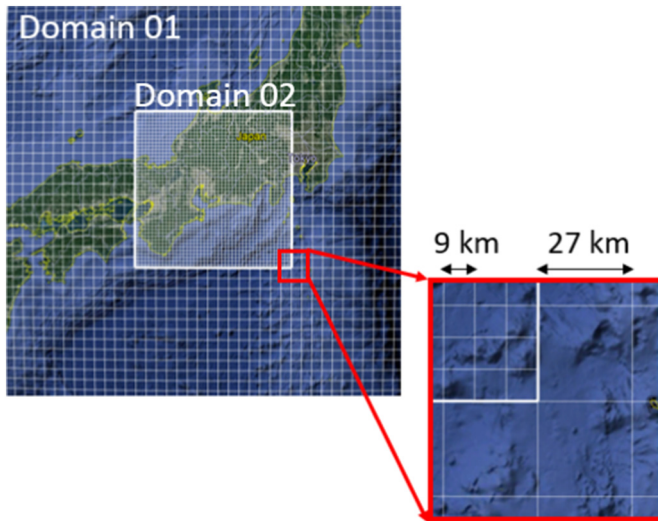
Fig. 2. Domains used in WRF-ARW simulation (upper: 27 km gridded domain, lower: domain 01 downscaled to 9 km gridded domain 02).

replaced with default USGS land use data which comes with the WRF model. In case 4, the second combination of the MYJ scheme and EMOS scheme was tested. For initial experiments (case 1–4), the coarse resolution 1° GFS LBC data was used with different combinations of PBL and surface layer schemes. While in the last case 5, the WRF simulations were conducted with the fine resolution 0.25° GFS LBC data with the combination of YSU and MOS schemes. Initially, all WRF tests were conducted for one month, i.e. January 2016. However, after determining the most suitable input datasets and WRF schemes, the final optimum case 5 was executed for an annual simulation.

2.3. Coastal ecosystem model configuration

To simulate the ecosystem, a modelling hydrodynamics framework and an ecosystem model was used, which is a combination of hydrodynamic, pelagic, and selectable benthic ecosystem models called the Ise Bay Simulator. The hydrodynamic model is a three-dimensional non-hydrostatic model with assumed incompressibility and Boussinesq approximation (Tanaka and Suzuki, 2010), and the pelagic ecosystem model contains a microbial process used to simulate the biogeochemical processes (Tanaka et al., 2011b). The model has been utilised for several ecosystem studies of semi-enclosed water bodies, not only for oxygen

Table 1
WRF-ARW model configuration.

Model	Advanced research WRF (ARW) Ver 4.0
Period	2016-01-01 to 2016-12-31
Horizontal resolution	Domain 01: 25 km × 25 km (40 × 40 grid points)
	Domain 02: 09 km × 09 km (46 × 46 grid points)
Vertical resolution	40 levels (surface to 10 hPa)
Static input data	USGS (1 km resolution)
(Land use data)	GSI (10 m resolution)
Dynamic input data	GFS-FNL.ds083.2 (1.0°)
(Lateral boundary condition)	NCEP-GDAS-FNL.ds.083.3 (0.25°)
PBL physics	Yonsei University Scheme (YSU)
	Mellor-Yamada-Janjic (Eta) TKE scheme
Surface layer schemes	Monin-Obukhov Similarity scheme
	Eta Monin-Obukhov (Janjic Eta) Similarity scheme
Land surface scheme	Noah land-surface model
Cumulus parameterisation	Grell 3D ensemble scheme
Long wave radiation scheme	RRTM
Short wave radiation schemes	RRTM
Microphysics	Thompson Graupel schemes
FDDA	Enable

Table 2
Experimental cases of weather simulations considering Yonsei University scheme (YSU), Mellor-Yamada-Janjic scheme (MYJ), Monin-Obukhov Similarity scheme (MOS) and Monin-Obukhov Janjic Eta Similarity scheme (EMOS). The static land use data from the geospatial authority of Japan (GSI) and the United States Geological Survey (USGS) is utilised. Four-dimensional data assimilation (FDDA) is enabled for most cases and dynamic lateral boundary condition (LBC) is taken from the Global Forecast System (GFS).

Case	PBL scheme	Surface layer scheme	Land use data	FDDA	LBC
1	YSU	MOS	GSI	Disable	GFS 1°
2	YSU	MOS	GSI	Enable	GFS 1°
3	YSU	MOS	USGS	Enable	GFS 1°
4	MYJ	EMOS	GSI	Enable	GFS 1°
5	YSU	MOS	GSI	Enable	GFS 0.25°

depletion (Tanaka et al., 2014), but also for food webs (Nagao and Nakamura, 2017), carbon cycle (Nagao et al. 2015), and blue tides (Yamamoto et al., 2015).

2.3.1. Physical hydrodynamic model

The physical hydrodynamic model consists of the basic continuity equation, momentum equations, sea state equation, and transport equation for scalar quantities such as water temperature and salinity. For the turbulence model, the large eddy simulation (LES) model (Smagorinsky, 1963) was used to calculate the horizontal turbulent kinematic viscosity and eddy diffusivity. A turbulent diffusion approach analytical model was used to calculate the diffusion coefficient and vertical eddy diffusivity in the vertical direction. This analytical model was originally developed by Henderson-Sellers for enclosed areas with the wind as a major source of mixing energy (Henderson-Sellers, 1985). This model was able to calculate diffusivity under any conditions of wind and stratification; however, a self-consistent formulation of the decay constant of the shear velocity with depth was an issue. This issue was resolved in a later refined version of this model (Nakamura and Hayakawa, 1991), which is adopted in this study.

2.3.2. Heat balance model

Shortwave radiation that permeates deeper water layers and the longwave radiation that is absorbed and released in the surface thin layer (approximately 10 μm) are considered the main heat balance variables as illustrated in Fig. 3. The heat balance at the water surface comprises of short-wave radiation Q_s, long-wave radiation Q_l, latent heat transfer Q_e, and sensible heat transfer Q_c. The net shortwave radiation Q_s on the water surface is the amount of solar incident radiation I_d[W m^{-2}] minus the water surface reflection accounted through albedo of water surface ($\alpha = 0.07$). The longwave radiation includes the amount reflected from the water surface to the sky L_u[W m^{-2}] and the amount that is reflected back to the water surface from the clouds L_d[W m^{-2}]. L_u is termed as longwave reverse radiation while L_d is termed as atmospheric radiation. The net longwave radiation Q_l at the water surface is the difference between L_u and L_d multiplied by the emissivity constant of longwave radiation ($\varepsilon = 0.96$).
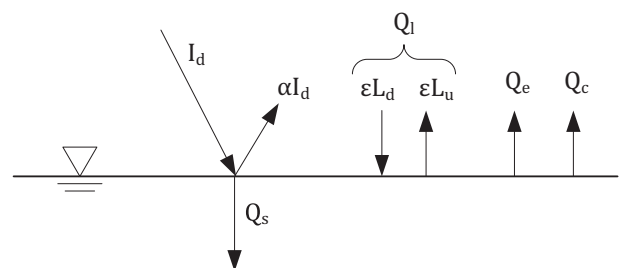

Fig. 3. Water surface heat balance with shortwave Q_s and longwave radiation Q_l as a positive term while sensible Q_c and latent heat Q_e as a negative term.

The radiation from the sky to the water surface is considered positive (downwards) and latent and sensible heats are taken negative in the opposite direction (upwards), then the heat balance equation at the water surface can be expressed as Eq. (1).

$$Q_n = Q_s + Q_l - Q_e - Q_c \tag{1}$$

Here, Q_n represents the net amount of heat at the water surface [W m^{-2}]. For a detailed mathematical formulation, see (Tanaka et al., 2014) and (Tanaka and Suzuki, 2010).

2.3.3. Pelagic and benthic ecosystem model

The Ise Bay Simulator is equipped with a detailed pelagic ecosystem model containing microbial processes and a benthic model to simulate biochemical processes (Tanaka et al., 2011b). This model can analyse several types of biological variables, such as phytoplankton, zooplankton, protozoa, and aerobic bacteria. In this study, phytoplanktons were further classified into four categories based on descending sizes: diatoms, dinoflagellates, autotrophic nanoflagellates (ANF), and Cyanobacteria. Protozoa were divided into two categories: ciliates and heterotrophic nanoflagellates (HNF). Zooplankton consisted of a single filter-feeding category and aerobic bacteria was also categorized into a single category. The Ise Bay Simulator classifies dissolved organic matter and suspended organic matter into C, N, and P and further classifies them into three categories based on the multi-G model (Westrich and Berner, 1984). The multi-G model classifies organic matter in multiple categories based on decomposition rate (degradable, quasi degradable, and persistent). The growth models for phytoplankton, bacteria, and DO showing its biochemical reactions are explained in Eqs. (2)–(4), for further details, see (Tanaka et al., 2014).

$$S_{PHY,i} = \overbrace{B_{PhyPS,i}}^{Photosynthesis} - \overbrace{B_{PhyExt,i}}^{Exteracellular\ release} - \overbrace{B_{PhyResp,i}}^{Respiration} - \overbrace{B_{PhyMor,i}}^{Natural\ Mortality}$$
$$- \overbrace{\sum_{j}^{N_{zoo}} B_{Phy2Zoo,i,j}}^{Grazing\ by\ Zooplankton} - \overbrace{\sum_{j}^{N_{PZ}} B_{Phy2Pz,i,j}}^{Grazing\ by\ Protozoa} + \overbrace{B_{PhyMig,i}}^{Vertical\ Migration} \tag{2}$$

where $S_{PHY,\ i}$ represents the change in local carbon source rate due to the biochemical change in phytoplankton.

$$S_{BAC,i} = \overbrace{B_{PhyPS,i}^{C}}^{Photosynthesis} - \overbrace{B_{BacResp,m}}^{Respiration} - \overbrace{B_{BacMor,m}}^{Natural\ Mortality} - \overbrace{\sum_{j}^{N_{zoo}} B_{Bac2Zoo,i,j}}^{Feeding\ by\ Zooplankton}$$
$$- \overbrace{\sum_{j}^{N_{PZ}} B_{Bac2Pz,i,j}}^{Feeding\ by\ Protozoa} \tag{3}$$

where $S_{BAC,\ i}$ represents the change in the local carbon source rate due to the biochemical change in bacteria.

$$S_{DO} = \overbrace{\sum_{i}^{N_{PHY}} TOD_C^{PHY,i}.B_{PhyPS,i}^C}^{Photosynthesis} - \overbrace{\sum_{i}^{N_{PHY}} TOD_C^{PHY,i}.B_{PhyResp,i}}^{Respiration\ of\ Phytoplankton} - \overbrace{\sum_{i}^{N_{ZOO}} TOD_C^{ZOO,i}.B_{ZooResp,i}}^{Respiration\ of\ Zooplankton}$$
$$- \overbrace{\sum_{i}^{N_{PZ}} TOD_C^{PZ,i}.B_{PzResp,i}}^{Respiration\ of\ Protozoa} - \overbrace{\sum_{i}^{N_{BAC}} TOD_C^{BAC,i}.B_{BacResp,i}}^{Respiration\ of\ Bacteria} - \overbrace{TOD_N^{NH4\ 2NO2}.B_{NH4\ 2NO2}}^{Nitrification}$$
$$- \overbrace{TOD_N^{NO4\ 2NO3}.B_{NO2\ 2NO3}}^{Nitrate\ Reduction} - \overbrace{TOD_S^{H2\ SOxi}.B_{H2\ SOxi}}^{Oxidation\ of\ Hydrogen\ Sulfide} \tag{4}$$

where S_{DO} represents the change in local oxygen source rate due to the biochemical change in DO; while total oxygen demand (TOD) values

related to phytoplankton, zooplankton, protozoa, and bacteria are in terms of O$_2$/Carbon ratios, and TOD values for nitrification, nitrate reduction and oxidation of hydrogen sulphide are in terms of O$_2$/Sulphur ratios. Fig. 4 shows the structure of the benthic flux model with key processes of oxygen consumption at the bottom sediments, denitrification, and the release of phosphorus, nitrogen, and hydrogen sulphide. The model mainly depends on the sedimentation flux of suspended organic matter and phytoplankton. As the organic matter settles as sediment, a part of it is assumed to be decomposed at a particular moment. The particulate organic carbon (POC) sediment flux changes to release the flux of hydrogen sulphide and the consumption flux of oxygen and nitrate in water immediately above. The particulate organic nitrogen (PON) and particulate organic phosphorus (POP) settling at the bottom are decomposed and are eventually converted into release fluxes of ammonium and phosphate.

The decomposition of POC that occurs through the consumption of oxygen (aerobic mineralisation) is modelled as Eq. (5), which is used to calculate sediment oxygen demand. The first part of the equation is a combination of two terms: the component of sediment flux, as DO demand for decomposing the settling organic matter from the pelagic model, and the background component as the DO demand for decomposing the settled organic matter before the start of the simulation, that is, the initial condition of sediment oxygen demand. The second part is modelled as a limiting function for linear change based on several trials. This limits oxygen consumption based on water temperature. This linear change is eventually modelled as Eq. (6) in several temperature intervals, for example, less consumption in the winter and more in the summer. In the case of Ise Bay, anoxia hardly occurs, and the average percentage of occurrence of denitrifying bacteria is only 0.11% compared to other heterotrophs (Sugahara et al., 1988). However, this modelling framework is capable of simulating anoxic conditions, followed by denitrification. The anaerobic decomposition of POC that occurs through nitrate reduction (denitrification) is modelled as Eq. (7). The denitrification process is limited by NO$_3$ concentration as well as oxygen concentration, and both limitations are modelled by Michaelis-Menten kinetics.

$$J_{DO}^{sed} = \overbrace{TOD_C^{POC}.\left(\frac{DO_w}{\left(K_{DO}^{sed} + DO_w\right)}\right).J_{POC}^{sed}}^{Component\ of\ Sediment\ Flux} + \overbrace{f_{liner}(T_i,f_i,n)}^{Background\ Component} \tag{5}$$

$$f_{liner}(T_i,f_i,n) = \begin{cases} f_1 & (T < T_1) \\ (1-t).f_i + t.f_{i+1}, \quad t = \dfrac{T-Ti}{T_{i+1}-T_i} & (T_i \leq T \leq T_{i+1}) \\ f_n & (T \geq T_n) \end{cases} \tag{6}$$

$$J_{NO_3}^{sed} = N_C^{Dec}.\overbrace{\left(\frac{NO_3}{\left(K_{NO_3}^{sed} + NO_3\right)}\right).\left(1 - \frac{DO_w}{\left(K_{DO}^{sed} + DO_w\right)}\right).J_{POC}^{sed}}^{Component\ of\ Sediment\ Flux} \tag{7}$$

where J_{DO}^{sed} represents the sediment oxygen demand, J_{POC}^{sed} symbolises the mineralisation of carbon with the sediment flux, $f_{liner}(T_i,f_i,n)$ denotes the limiter function for background oxygen consumption, T_i is the increasing temperature with corresponding oxygen consumption f_i for n intervals, TOD_C^{POC} is in terms of O$_2$/Carbon ratios, K_{DO}^{sed} and $K_{NO_3}^{sed}$ is the half-saturation constant of DO and nitrate, and DO_w is the DO concentration of the overlying water just above the sediment surface. $J_{NO_3}^{sed}$ represents the sediment flux of nitrate and N_C^{Dec} represents the nitrate required for the decomposition of POC. NO_3 is the nitrate concentration of the overlying water just above the sediment surface. A similar equation for the mineralisation reaction using sulphuric acid was also considered. Table 3 summarises the whole configuration of the ecosystem model used in this study.
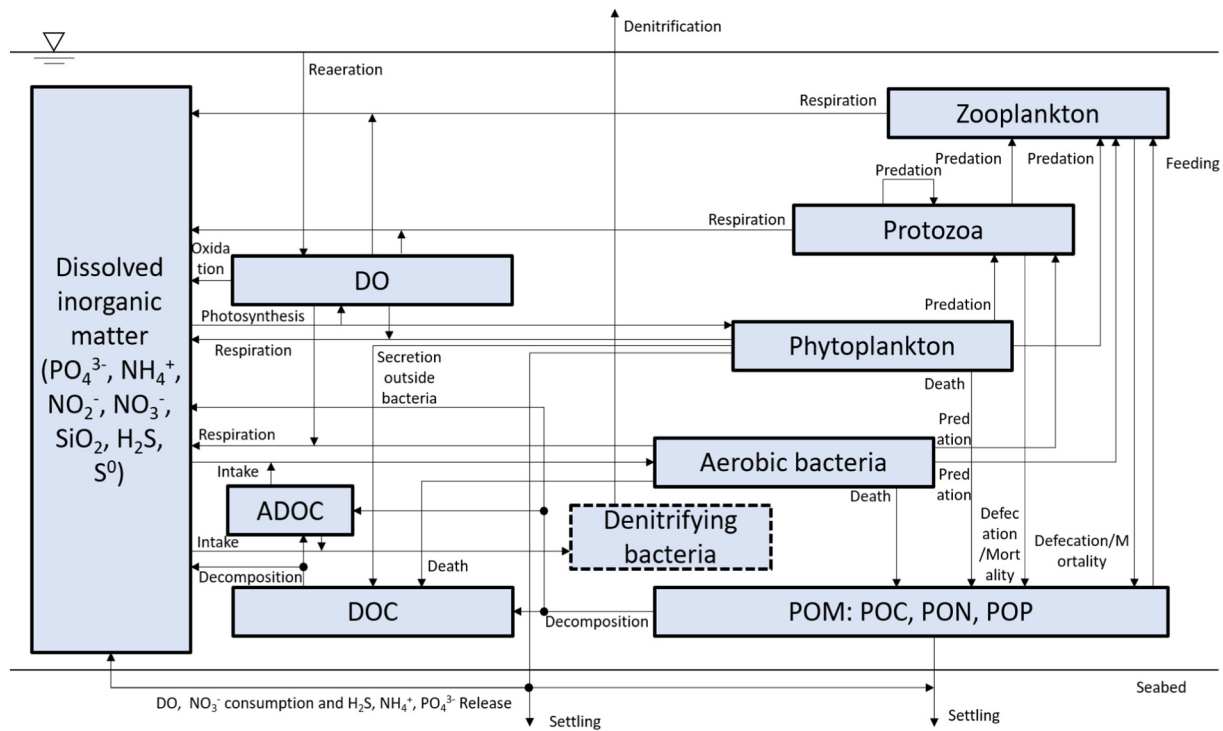
Fig. 4. Structure of the benthic flux ecosystem model.

2.3.4. Observed data

To verify the hydrodynamic simulations, the temperature and salinity of the surface (1 m) and bottom-layer water (25 m) were compared with the observed data at the head buoy and the open ocean buoy, respectively (see Fig. 1). Similarly, to verify the ecosystem results the observed bottom DO was also compared with the simulated DO. Both buoys are equipped with multiple sensors for measuring depth, water temperature, salinity and DO at 1-hour intervals. The data used are open-source and were obtained from the Ise bay environmental database operated by the MILT ('Isewan Environmental Database,' n.d.). WRF and AMeDAS precipitation products were also compared in terms of river discharge owing to their direct relationship with nutrient loading into Ise Bay. A total of 10 first-class rivers were evaluated for river discharge. The river discharge referred to as 'observed' was not directly observed but it was calculated from the rating curves based on the observed water levels. These rating curves were based on observations made by the Ministry of Land, Infrastructure, Transport, and Tourism (MLIT). These rating curves were used in the hydrodynamic and ecosystem simulations of Ise Bay in the past and promising salinity results revealed their indirect reliability (Tanaka et al., 2011a).

3. Results and discussion

3.1. Weather simulation

Table 4 summarises the coefficient of determination (R^2) of all the cases tested to obtain the most appropriate model configuration and input datasets for Ise Bay. Case 1 resulted in a very low R^2 value for both air temperature and wind speed. In case 2, all WRF settings were fixed as in case 1, except that the FDDA option was enabled, which helped to improve the R^2 value for both variables due to lesser model deviations from the input boundary data. Following the improvement in case 2 due to enabling of FDDA, the accurate topography and land use data from GSI were replaced with USGS data in case 3, and it was evident from the air temperature and wind simulation results that it had no significant impact on the air temperature and wind speed at the sea surface. However, for subsequent cases (4–5), high resolution and more accurate land use data of GSI were used instead of USGS data. The second combination of the WRF PBL scheme and surface layer scheme (Mellor-Yamada-Janjic, Eta TKE scheme & Eta Monin-

Table 3
Configuration of the coastal ecosystem model.

Model	Ise bay simulator
Period	2016-01-01 to 2016-12-31
Grids	Horizontal: 800 m × 800 m (85 × 85 grid points) Vertical: 33 layers (−90–5 m)
Biological variables	Phytoplankton (diatom, dinoflagellate, ANF, cyanobacteria), Zooplankton, protozoa (ciliate, HNF), and aerobic bacteria.
Horizontal turbulence model	Sub grid-scale model (SGS)
Vertical turbulence model	Nakamura model (Improved Henderson-Sellers Model)
Input data	Tides: hourly tides observed at Toba tide gauge. Open ocean boundary data: hourly water quality profile observed at Open ocean monitoring buoy. River discharge: observed and based on rating curves. Weather data: air temperature, solar radiation, wind velocity, wind direction & precipitation. Nutrient loading: calculated from the empirical equation (Gunnerson, 1967).

Table 4
WRF simulation cases with corresponding R^2 values.

Case	R^2	
	Temperature	Wind
1	0.38	0.46
2	0.64	0.65
3	0.64	0.65
4	0.50	0.64
5	0.86	0.60

Obukhov, Janjic Eta Similarity scheme) was tested in case 4, and it was found that the R^2 for air temperature significantly decreased from 0.64 to 0.50. This is due to the overestimation of the air temperature by the Mellor Yamada scheme owing to the inhibited vertical mixing in the PBL layer. Case 5 shows the final WRF settings with the best combination of PBL and the surface layer scheme obtained from the previous test cases. More accurate LBC data with 0.25° resolution was also replaced in case 5 with the 1° GFS data, which provided the most accurate simulation results for air temperature and reasonably good results for wind speed. The replacement of input LBC files and WRF schemes proved to be the most influential factor in improving simulation accuracy.

Fig. 5 shows the comparison of daily means of air temperature and wind speed for the year 2016, at the Chubu Centrair weather station. The air temperature was perfectly simulated with an R^2 value of 0.97 ($r = 0.99$, $p < 0.001$). The simulated yearly mean value for air temperature was almost equal to the observed yearly mean value. The overall R^2 value of 0.69 ($r = 0.84$, $p < 0.001$) was achieved in the case of wind speed. The WRF underestimated the wind speed of strong winter events but accurately reproduced the summer wind speed, which is of prime interest in this study because hypoxia is typically prevalent in this season.

The simulation results were not only compared for wind speed but also wind direction, as it is equally important for the coastal ecosystem
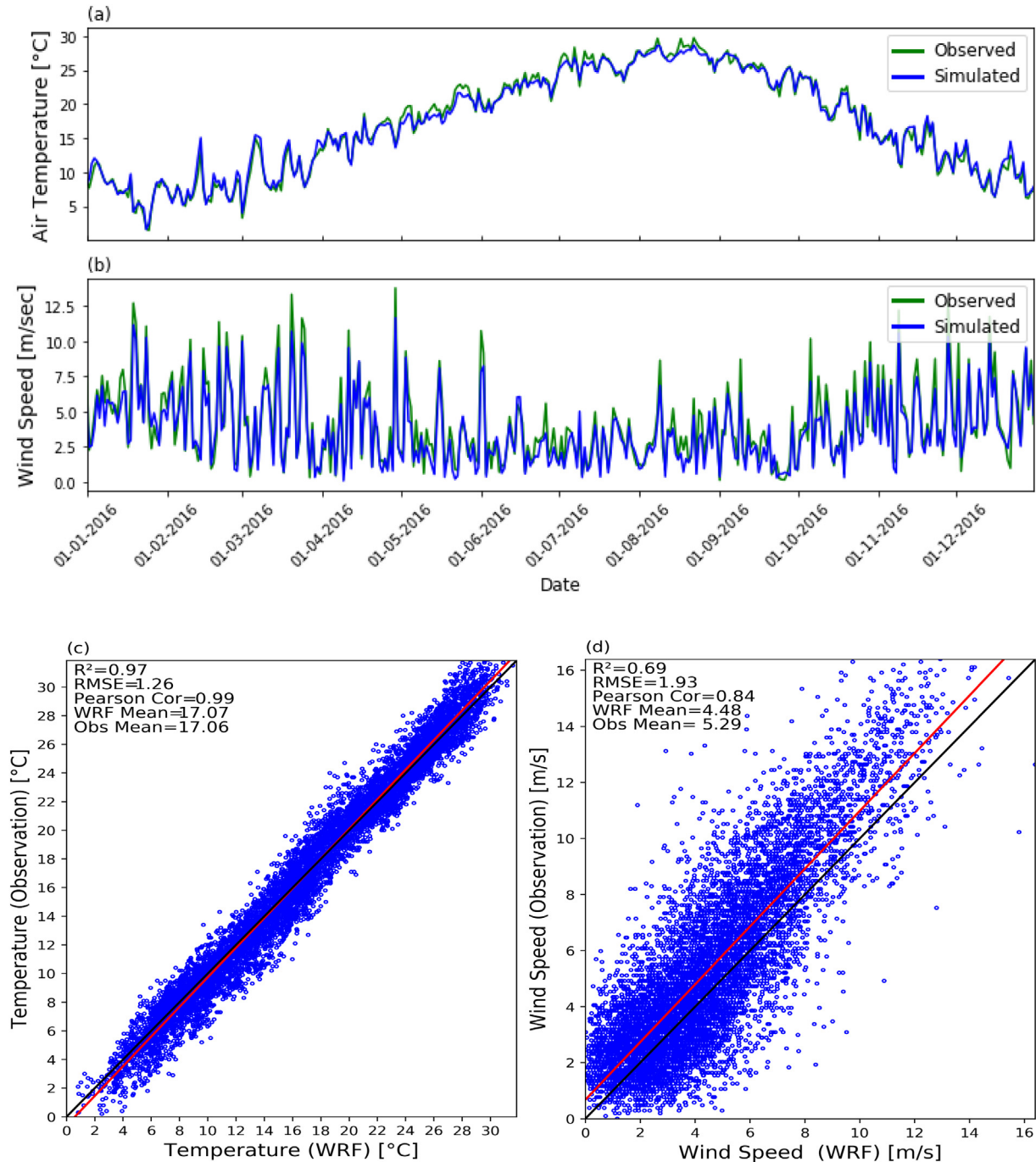
Fig. 5. (a & b) Timeseries comparison of simulated air temperature and wind speed at Chubu Cetrair weather station for the year 2016; (c) comparison between observed and simulated temperature; (d) comparison between observed and simulated wind speed. The red lines denote the regression fit between simulation and observation.
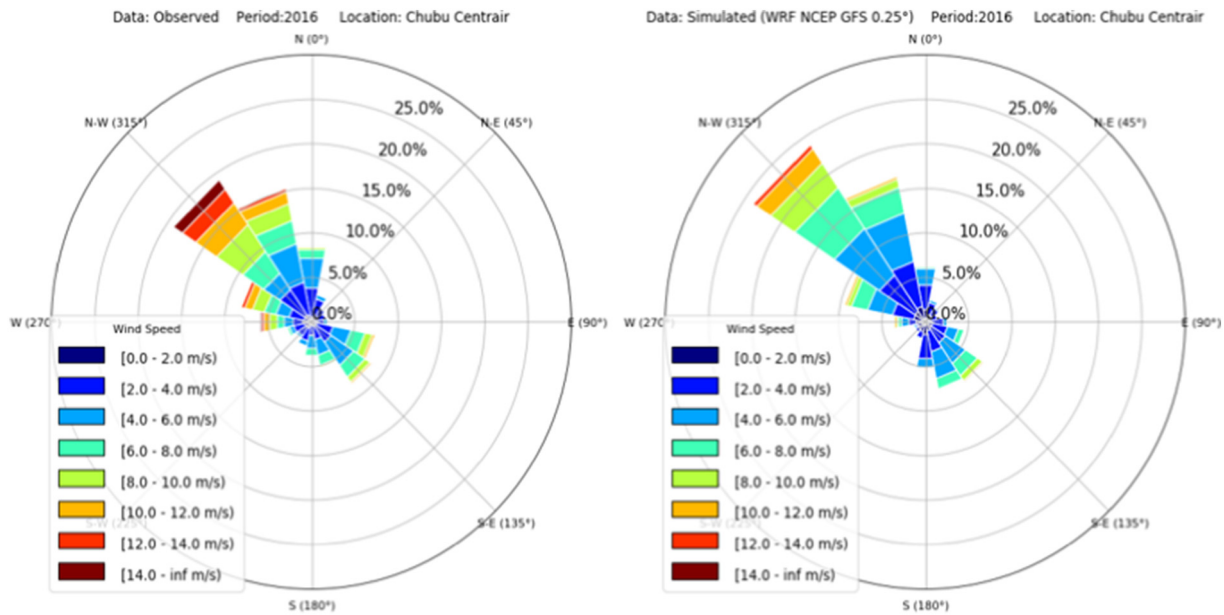
Fig. 6. (Left) Windrose plot for observed wind speed and direction at Chubu Centrair weather station. (Right) Windrose plot for simulated wind speed and direction at the same station.

model. Fig. 6 shows the wind rose plots prepared for both observed (left) and simulated (right) wind speed and directions. This figure gives a succinct view of how wind speed and direction are distributed at the Chubu Centrair weather station during the whole year. The simulated wind direction was fairly consistent with the observed and typical wind pattern of Ise Bay, which is NW dominant in the winter, and SE dominant in the summer season. However, the percentage of NW low wind speed events increased in the simulation as compared to the observation. A similar pattern was also observed with high wind speed (≥12 m/s) events.

The river discharge from the WRF and AMeDAS precipitation products was calculated using a lumped tank hydrological model based on the Parasad three-parameter storage function model (Padiyedath Gopalan et al., 2018; Parasad, 1967). Fig. 7 shows a comparison between the observed and simulated total discharge of 5 major rivers (Kiso River, Suzuka River, Ibi River, Nagara River, Syonai River). The AMeDAS river discharge was slightly overestimated with an R^2 score of 0.70, while WRF-based river discharge was underestimated with an R^2 score of 0.60.

3.2. Ecosystem simulation

3.2.1. Reproducibility of surface and bottom water temperature and salinity

To assess the accuracy of the hydrodynamic simulations, a comparison between simulated and observed water temperature and salinity was made for both the surface and bottom layers at the location of a head buoy and open ocean buoy.

The hourly means of simulation results were in good agreement with the observed data for both the AMeDAS- and WRF-driven simulations, as shown in Fig. 8. In the case of temperature and salinity, the WRF-driven simulations performed relatively well and were in good agreement with the observations. However, there were some inconsistencies found in the AMeDAS results, especially on the surface and bottom layer of the head buoy, which was attributed to overestimation of river discharge and higher wind speed as compared to WRF weather data. The head buoy is located near the head of the bay and is significantly influenced by higher river discharge events as the three major Kiso rivers flow into Ise Bay from this direction.
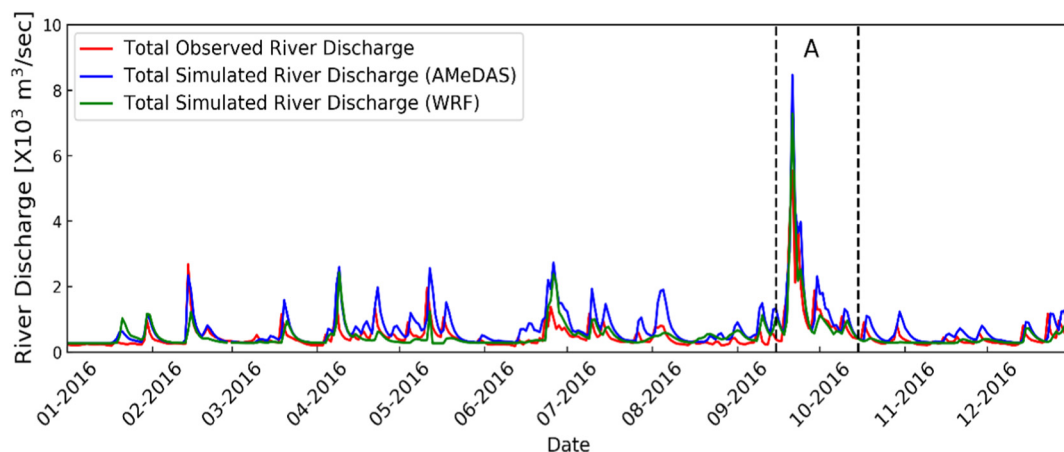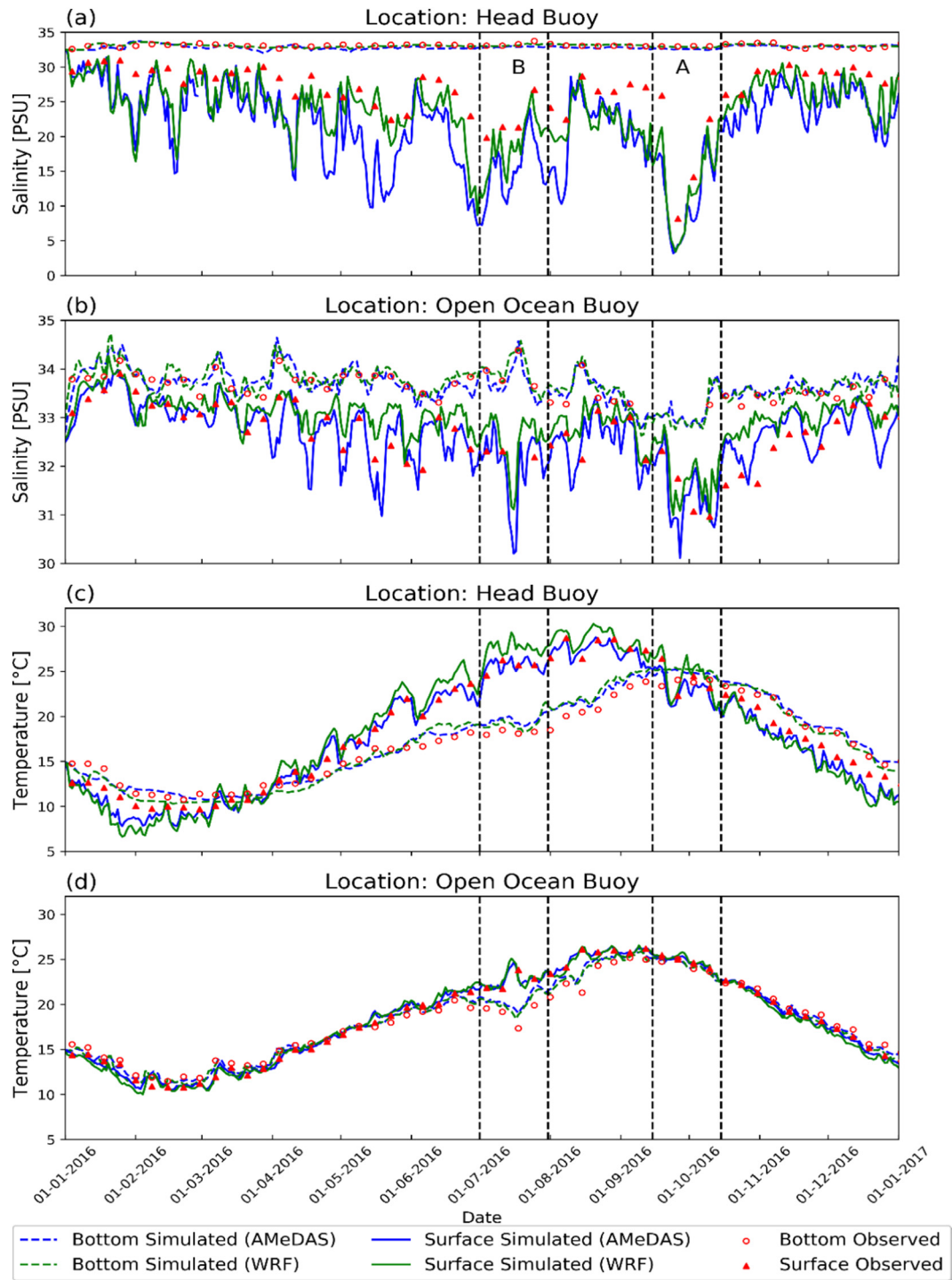

Fig. 7. Comparison of river discharge calculated from 5 first-class rivers using AMeDAS and WRF precipitation products. The vertical dashed lines represent the peak river discharge as period (A).

Fig. 8. (a & b) Timeseries comparison between simulated and observed salinity at the head and open ocean buoys, (c & d) comparison between observed and simulated water temperature at the head and open ocean buoys. The vertical dashed lines covering July highlight the intrusion of oceanic water into the bay as period (B), while vertical dashed lines from September highlights the peak river discharge as period (A).

The intrusion of oceanic water into the bay in July (see period 'B' in Fig. 8), which led to a decline in water temperature and an increase in salinity at the head buoy, was also well reproduced in both simulations. Similarly, the end of September higher river discharge event from the bay head (see period 'A' in Figs. 7 and 8), which led to a decline in surface water temperature and salinity was also well reproduced in both simulations for the region of freshwater influence (ROFI), i.e. head buoy. Overall, the intrusion events as well as peak river discharge events that often impact the coastal environment were well simulated and adequately reflected the actual conditions.

3.2.2. Reproducibility of bottom water DO findings

The core objective of this study was to simulate bottom-layer DO conditions as it is one of the most important parameters directly associated with the health of coastal environments. DO reproducibility is relatively difficult to achieve as compared to water temperature and salinity, as it is sensitive to both physical and biogeochemical processes. Bottom DO was compared at the head and open ocean monitoring buoys to assess the model performance in shallow and deep waters. The comparison was made from the beginning of March to the end of September, covering the hypoxic period. The first two months (January
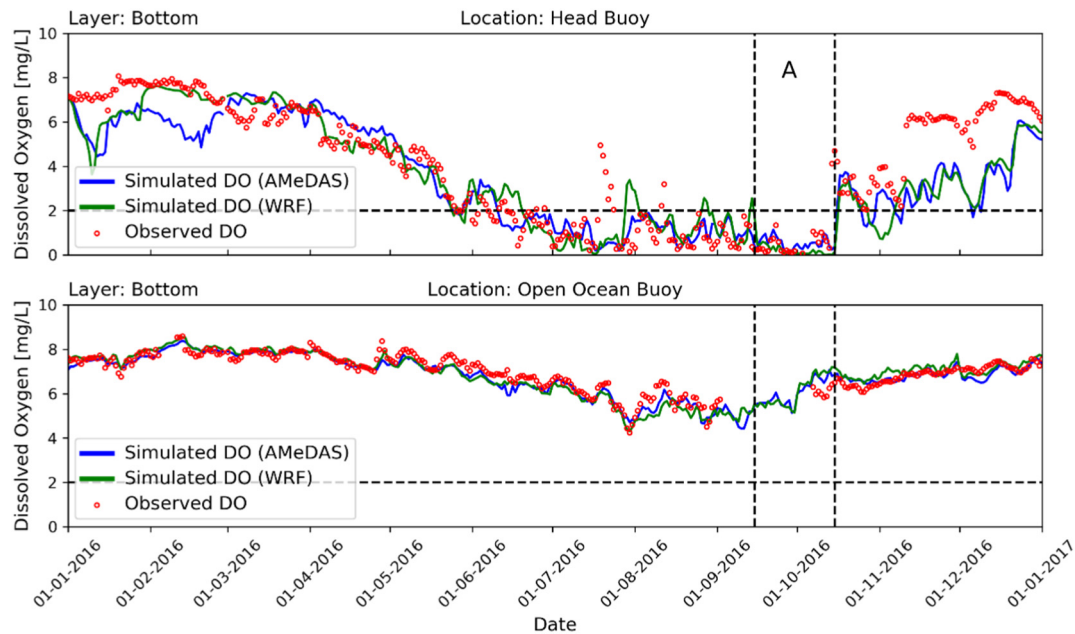
Fig. 9. (Upper) Timeseries of the observed (red dots), AMeDAS-driven (blue line), and WRF-driven (green line) bottom DO at the head buoy. (Lower) Timeseries of the observed (red dots), AMeDAS-driven (blue line), and WRF-driven (green line) bottom DO at the open ocean buoy. The vertical dashed lines correspond to the peak river discharge period (A).

and February) of the simulation were considered as a spin-up period. Fig. 9 shows the comparison between the simulated bottom DO and the observed DO for the AMeDAS and WRF-driven simulation. It was found that the model performed reasonably well under both meteorological forcings. Table 5 summarises the performance evaluation of both meteorological forcings. R^2, root mean square error (RMSE), and percentage bias (PBIAS) were used as performance indicators, and it was evident from R^2 value that more than 85% and 90% of the DO variance was well captured by the model for the head and open ocean buoy, respectively. The RMSE value was also less than 1 mg/L for both monitoring stations.

The seasonality in the bottom DO was also well replicated by both simulations with an accuracy of 80% and 90% for the head and open ocean buoy, respectively. Seasonal and short-term variations around 2 mg/L and the sudden recovery of the bottom DO in the middle of October were well reproduced. Quick recovery of bottom DO coincided well with the increase in bottom salinity as well as the end of freshwater discharge (See Period 'A' in Fig. 7). This was attributed to the intrusion of a dense oxygen-rich water mass.

To examine the slight differences in both simulations (AMeDAS and WRF), the simulated total particulate organic content was also compared. Total POC was calculated by adding the carbon content of all four types of phytoplankton, zooplankton, two types of protozoa, and all three types of POC based on the Multi-G model. Fig. 10 shows the comparison between the simulated POC for the AMeDAS- and WRF-

driven simulations at the two buoy locations. The AMeDAS simulated POC was slightly higher than that of WRF at both locations. This was attributed to a higher river discharge, which yielded excessive nutrients loading (see Table 6) as compared to WRF and eventually yielded more oxygen uptake at the bottom.

To assess the accuracy of DO simulations, hypoxic days were further calculated for three thresholds DO levels (≤2, ≤3, and ≤4 mg/L) at the head buoy, and it was found that both AMeDAS and WRF performed reasonably well to simulate hypoxic events. Table 6 shows the comparison between the simulated and observed hypoxic days and nutrients loading. The hypoxic day was defined as a day when the DO at the bottom fell below the given threshold DO value. The observed hypoxic days for ≤3 mg/L and ≤4 mg/L thresholds were in good agreement with both AMeDAS- and WRF-driven simulations. The ≤2 mg/L threshold hypoxic days were higher in AMeDAS as compared to observed and WRF-driven simulation. This shows that hypoxic water mass stayed for a longer period in the AMeDAS simulation because more hypoxic conditions were available due to higher riverine inputs and nutrient loadings.

Bottom DO depletion is a notable global issue that has been a target of water quality criteria. For example, in April 2003, the U.S. Environmental Protection Agency (USEPA) published the ambient water quality criteria for DO, water clarity, and chlorophyll-*a* for the Chesapeake Bay and its tidal tributaries (USEPA, 2003). It was the foundation document defining the Chesapeake Bay water quality criteria and recommended implementation procedures for monitoring and assessment. The Japanese Government also revised the water quality standards in 2016 and added bottom DO as a new standard. In addition to water quality standards, the government also formulated pollutant load control plans to reduce nutrient loading under different management scenarios. To meet the requirements of achieving these objectives, both continuous monitoring of water quality and benthic fauna and the modelling approach are useful. As weather conditions greatly affect water quality and its distribution, such as hypoxia/anoxia, it is always difficult to extract the causal chain of hypoxia development from field observation/monitoring data alone. Therefore, for practical and scientific research, establishing a sound modelling framework is essential.

Ise Bay is a rich fishery resource; however, the fish catch of bottom otter trawling in Ise Bay has greatly decreased from approximately 7200 tons in 2000 to about 4600 tons in 2009. These changes in fish catches were attributed to environmental variables such as water

Table 5
Performance evaluation of both meteorological forcings to simulate the bottom DO. A regression comparison was made from the beginning of March to the end of September, covering the hypoxic period.

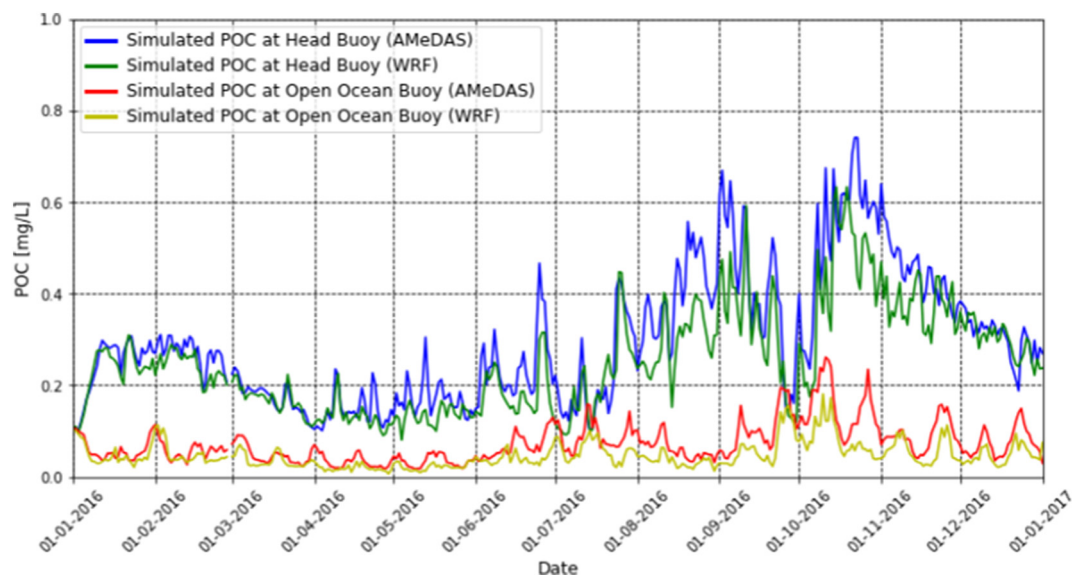| Meteorological forcing	Bottom dissolved oxygen (March–September)					
	R^2	Pearson correlation	RMSE	PBIAS	Simulation mean	Observation mean
Location: head buoy						
AMeDAS	0.88	0.94	0.87	−14.60	3.02	2.84
WRF	0.83	0.91	0.96	−12.74	2.99	2.84
Location: open ocean buoy						
AMeDAS	0.92	0.96	0.33	−1.44	6.50	6.86
WRF	0.91	0.95	0.39	−0.49	6.46	6.86

Fig. 10. Simulated total surface POC at the head and open ocean buoys.

temperature and DO (Iwaba et al., 2019). Therefore, understanding environmental conditions, especially DO variation, is very important for the resource management of fisheries. The development of this rigorous framework has proven to be a useful tool to simulate bottom DO with high accuracy.

Currently, historical weather products were utilised in this study to simulate the bottom DO. In the future, GCM outputs under changing climate and Representative Concentration Pathway (RCP) scenarios will be integrated into this modelling framework. This will help us understand the future temporal and spatial variation of coastal hypoxia under climate change. The WRF model generates the metrological boundary data to drive the hydrodynamic and coastal ecosystem models. The capability of the model can be further explored with data assimilation methodologies to make use as a short-term forecasting model for hypoxic conditions as necessary meteorological forcing's can be obtained from NCEP-FNL atmospheric data, which are available on a global scale for short-term forecasts.

4. Conclusions

In this study, an integrated modelling framework was developed. The modelling framework consisted of the WRF model, 3D hydrodynamic model, and a coastal ecosystem model to simulate the physical and biochemical processes, including DO dynamics and seasonal hypoxia. The modelling framework was applied to a research site in Japan, named Ise Bay. The targeted research site suffers from seasonal hypoxia and is the major cause of mass fish kills every year. The biomass of megabenthos and the richness of the main mega benthos species are also severely affected in every hypoxic season. Through the calibration and validation of the reproducibility of the weather, hydrodynamic,

and ecosystem models and their combination, the method established in this study was proven to be highly reliable.

The hydrodynamic model results based on a simulation in 2016 show that water temperature and salinity of the surface and bottom layers were well reproduced in both the AMeDAS- and WRF-driven simulations. However, in the case of the AMeDAS-driven simulation, some perturbations were found in the surface and bottom-layer salinity attributed to overestimated river discharge and wind speed. The ecosystem model results show that the hypoxic period in the shallow water started in the middle of June and ended in the middle of October. Overall, the performance of both datasets (AMeDAS and WRF) was equally good in the summer hypoxic season. Moreover, >80% and >90% of the DO variance was reproduced for shallow and deep water, respectively. However, for the autumn season, the bottom DO in the shallow water was underestimated, which was due to the temperature-dependent background sediment oxygen demand function. As the water temperature ranges for the autumn and spring seasons fall within the same range, equal background sediment oxygen demand was applied. Moreover, the dominance of the sediment oxygen demand for DO depletion at the bottom affected shallow water as compared to deep water.

CRediT authorship contribution statement

Muhammad Ali Hafeez: Conceptualization, Methodology, Investigation, Validation, Writing – original draft, Visualization. **Yoshiyuki Nakamura:** Conceptualization, Methodology, Resources, Writing – review & editing. **Takayuki Suzuki:** Methodology, Writing – review & editing. **Tetsunori Inoue:** Methodology, Resources, Writing – review & editing. **Yoshitaka Matsuzaki:** Methodology, Resources, Writing – review & editing. **Kangnian Wang:** Methodology, Writing – review & editing. **Abdul Moiz:** Methodology, Writing – review & editing.

Declaration of competing interest

The authors declare that they have no conflict of interest.

Acknowledgments

Table 6
Comparison of observed and simulated hypoxic days and nutrients loading.

Meteorological forcing	Hypoxic days (March–September)			Nutrients loading (ton/day)	
	≤2 mg/L	≤3 mg/L	≤4 mg/L	TN	TP
Observed	108	127	136	102.33	5.43
AMeDAS	116	131	140	131.67	8.27
WRF	99	126	146	90.01	5.7

References

Blumberg, A.F., Mellor, G.L., 1987. A description of a three dimensional coastal ocean circulation model. Coast. Estuar. Sci. 4.

Burt, K., Hamoutene, D., Mabrouk, G., Lang, C., Puestow, T., Drover, D., Losier, R., Page, F., 2012. Environmental conditions and occurrence of hypoxia within production cages of Atlantic salmon on the south coast of Newfoundland. Aquac. Res. 43, 607–620. https://doi.org/10.1111/j.1365-2109.2011.02867.x.

Carstensen, J., Andersen, J.H., Gustafsson, B.G., Conley, D.J., 2014. Deoxygenation of the Baltic Sea during the last century. Proc. Natl. Acad. Sci. U. S. A. 111, 5628–5633. https://doi.org/10.1073/pnas.1323156111.

Chen, F., Dudhia, J., 2001. Coupling an advanced land surface–hydrology model with the Penn State–NCAR MM5 modeling system. Part I: Model Implementation and Sensitivity. Mon. Weather Rev. 129, 569–585.

Chen, F., Janjić, Z., Mitchell, K., 1997. Impact of atmospheric surface-layer parameterizations in the new land-surface scheme of the NCEP mesoscale Eta model. Boundary-Layer Meteorol. 85, 391–421. https://doi.org/10.1023/A:1000531001463.

De Meij, A., Vinuesa, J.F., 2014. Impact of SRTM and Corine Land Cover data on meteorological parameters using WRF. Atmos. Res. 143, 351–370. https://doi.org/10.1016/j.atmosres.2014.03.004.

Diaz, R.J., Rosenberg, R., 2008. Spreading dead zones and consequences for marine ecosystems. Science (80-.). 321, 926–929. doi:https://doi.org/10.1126/science.1156401.

Fujiwara, T., Takahashi, T., Kasai, A., Sugiyama, Y., Kuno, M., 2002. The role of circulation in the development of hypoxia in Ise Bay. Japan. Estuar. Coast. Shelf Sci. 54, 19–31. https://doi.org/10.1006/ecss.2001.0824.

Galán, A., Zirbel, M.J., Saldías, G.S., Chan, F., Letelier, R., 2020. The role of upwelling intermittence in the development of hypoxia and nitrogen loss over the Oregon shelf. J. Mar. Syst. 207, 103342. https://doi.org/10.1016/j.jmarsys.2020.103342.

Galgani, L., Stolle, C., Endres, S., Schulz, K.G., Engel, A., 2014. Effects of ocean acidification on the biogenic composition of the sea-surface microlayer. J. Geophys. Res. Ocean. 119, 7911–7924. https://doi.org/10.1002/2014JC010188.Received.

Gamperl, A.K., Ajiboye, O.O., Zanuzzo, F.S., Sandrelli, R.M., de Peroni, E.F.C., Beemelmanns, A., 2020. The impacts of increasing temperature and moderate hypoxia on the production characteristics, cardiac morphology and haematology of Atlantic Salmon (Salmo salar). Aquaculture 519, 734874. https://doi.org/10.1016/j.aquaculture.2019.734874.

Ganmanee, M., Narita, T., Sekiguchi, H., 2003. Some aspects of population dynamics of asteroid luidia quinaria in Ise Bay. Central Japan. Benthos Res. 58, 31–42.

Grell, G.A., Freitas, S.R., 2013. A scale and aerosol aware stochastic convective parameterization for weather and air quality modeling. Atmos. Chem. Phys. Discuss. 13, 23845–23893. https://doi.org/10.5194/acpd-13-23845-2013.

Gunnerson, C.G., 1967. Streamflow and quality in the Columbia River Basin. J. Sanit. Eng. Div. 93, 1–16.

Hafeez, M.A., Nakamura, Y., Inoue, T., Hosokawa, S., Matsuzaki, Y., 2019. Quantification of bottom water age by using temperature based age index model and its relationship with bottom water dissolved oxygen concentration in Ise Bay, Japan. J. Japan Soc. Civ. Eng. Ser. B2 (Coastal Eng. 75, I_1003-I_1008. doi:https://doi.org/10.2208/kaigan.75.i_1003.

Hafeez, M.A., Nakamura, Y., Inoue, T., Hosokawa, S., Matsuzaki, Y., 2020. Seasonal variation in intrusion frequency of oceanic water from middle and lower layers and its significance in bottom water hypoxia in Ise Bay, Japan, in: Apac 2019. Springer, pp. 1043–1050. doi:https://doi.org/10.1007/978-981-15-0291-0.

Harada, M., 2008. Present status and problems of penaeid shrimps and mantis shrimp resources of the small-scale bottom trawl in Ise Bay and Enshu Nada. Fish. Biol. Oceanogr. Kuroshio 9, 9–13 (In Japanese).

Henderson-Sellers, B., 1985. New formulation of eddy diffusion thermocline models. Appl. Math. Model. 9, 441–446.

Hong, S.Y., 2010. A new stable boundary-layer mixing scheme and its impact on the simulated East Asian summer monsoon. Q. J. R. Meteorol. Soc. 136, 1481–1496. https://doi.org/10.1002/qj.665.

Hong, S.Y., Noh, Y., Dudhia, J., 2006. A new vertical diffusion package with an explicit treatment of entrainment processes. Mon. Weather Rev. 134, 2318–2341. https://doi.org/10.1175/MWR3199.1.

Hossain, M., Sekiguchi, H., 1996. Influence of oxygen poor water on megabenthos communities in Ise Bay. Centeral Japan. Bull. Japanese Soc. Fish. Oceanogr. 60, 237–243.

Iacono, M.J., Mlawer, E.J., Clough, S.A., 2001. Validation of the RRTM shortwave radiation model and comparison to GCM shortwave models. Elev. ARM Sci. Team Meet. Proc. 2, 1–6.

Isewan Environmental Database 2021 [WWW Document], n.d. URL http://www.isewandb.go.jp/ (accessed 9.1.18).

Iwaba, K., Tabeta, S., Hamada, T., Maruyama, T., Tachi, H., 2019. Environmental monitoring using small fishing boats in Ise Bay for fishery management. Estuar. Coast. Shelf Sci. 228, 1–7. https://doi.org/10.1016/j.ecss.2019.106387.

Janjic, Z.I., 1990. The step-mountain coordinate: physical package. Mon. Weather Rev. https://doi.org/10.1175/1520-0493(1990)118<1429:TSMCPP>2.0.CO;2.

Jiménez, P.A., Dudhia, J., González-Rouco, J.F., Navarro, J., Montávez, J.P., García-Bustamante, E., 2012. A revised scheme for the WRF surface layer formulation. Mon. Weather Rev. 140, 898–918. https://doi.org/10.1175/MWR-D-11-00056.1.

Jiménez-Esteve, B., Udina, M., Soler, M.R., Pepin, N., Miró, J.R., 2018. Land use and topography influence in a complex terrain area: a high resolution mesoscale modeling study over the Eastern Pyrenees using the WRF model. Atmos. Res. 202, 49–62. https://doi.org/10.1016/j.atmosres.2017.11.012.

Kasai, A., 2014. Hypoxia controlled by hydrodynamics. Aqua-Bioscience Monogr. 7, 117–145. https://doi.org/10.5047/absm.2014.00704.0117.

Kasai, A., Fujiwara, T., Kimura, T., Yamada, H., 2004. Fortnightly shifts of intrusion depth of oceanic water into Ise Bay. J. Oceanogr. 60, 817–824. https://doi.org/10.1007/s10872-004-5774-x.

Katin, A., Del Giudice, D., Obenour, D.R., 2019. Modeling biophysical controls on hypoxia in a shallow estuary using a Bayesian mechanistic approach. Environ. Model. Softw. 120, 104491. https://doi.org/10.1016/j.envsoft.2019.07.016.

Keister, J.E., Houde, E.D., Breitburg, D.L., 2000. Effects of bottom-layer hypoxia on abundances and depth distributions of organisms in Patuxent River, Chesapeake Bay. Mar. Ecol. Prog. Ser. 205, 43–59. https://doi.org/10.3354/meps205043.

Loveland, T.R., Reed, B.C., Ohlen, D.O., Brown, J.F., Zhu, Z., Yang, L., Merchant, J.W., 2000. Development of a global land cover characteristics database and IGBP DISCover from 1 km AVHRR data. Int. J. Remote Sens. 21, 1303–1330. https://doi.org/10.1080/014311600210191.

Matear, R.J., Hirst, A.C., 2003. Long-term changes in dissolved oxygen concentrations in the ocean caused by protracted global warming. Global Biogeochem. Cycles 17, n/a-n/a. doi:https://doi.org/10.1029/2002gb001997.

Matsuzaki, Y., Fujiki, T., Kawaguchi, K., Inoue, T., Iwamoto, T., 2020. Application of the WRF model to the coastal area at Ise Bay, Japan: evaluation of model output sensitivity to input data. Coast. Eng. J. 00, 1–15. https://doi.org/10.1080/21664250.2020.1830485.

Mellor, G.L., Yamada, T., 1982. Development of a turbulence closure model for geophysical fluid problems. Rev. Geophys. 20, 851–875. https://doi.org/10.1029/RG020i004p00851.

Minamiguchi, Y., Shimadera, H., Matsuo, T., Kondo, A., 2018. Numerical simulation of heavy rainfall in August 2014 over Japan and analysis of its sensitivity to sea surface temperature. Atmosphere (Basel). 9. https://doi.org/10.3390/atmos9030084.

Mlawer, E.J., Taubman, S.J., Brown, P.D., Iacono, M.J., Clough, S.A., 1997. Radiative transfer for inhomogeneous atmospheres: RRTM, a validated correlated-k model for the longwave. J. Geophys. Res. D Atmos. 102, 16663–16682. https://doi.org/10.1029/97jd00237.

Monin, A.S., Obukhov, A.M., 1959. Basic laws of turbulent mixing in the surface layer of the atmosphere 24, 163–187.

Nagao, K., Nakamura, Y., 2017. Modelling Microbial Food Webs in Ise-Bay. J. Japan Soc. Civ. Eng. Ser. B2 (Coastal Eng. 73, 1327-1332) (In Japanese).

Nakamura, Y., Hayakawa, N., 1991. Modelling of thermal stratification in lakes and coastal seas. Hydrol. Nat. manmade lakes. Proc. Symp. Vienna 1991, 227–236.

Nakao, T., Matsuzaki, K., 1995. Potential for eutrophication based on the topography of coastal bays. Oceanogr. Japan 4, 19–29 (In Japanese).

Narita, T., Hossain, M., Sekiguchi, H., 2003. Seasonal and interannual variations in biomass and abundance of megabenthos in Ise Bay. Central Japan. Benthos Res. 58, 75–85. https://doi.org/10.5179/benthos1996.58.1_75.

Narita, T., Ganmanee, M., Sekiguchi, H., 2006. Population dynamics of a dragonet Repomucenus valenciennei in Ise Bay, central Japan. Nippon Suisan Gakkaishi 72, 860–872 (In Japanese).

NCEP FNL 1 Degree, 2021 DOI:https://doi.org/10.5065/D6M043C6 [WWW Document], n. d. URL doi:https://doi.org/10.5065/D6M043C6 (accessed 9.1.18).

NCEP GDAS/FNL 0.25 Degree, 2021 DOI:10.5065/D65Q4T4Z [WWW Document], n.d. Natl. Cent. Atmos. Res. Comput. Inf. Syst. Lab. URL doi:https://doi.org/10.5065/D65Q4T4Z (accessed 9.1.18).

Nagao, K., Tanaka, Y., Nakata, K., Onda, M., 2015. Analysis of carbon cycle considering microbial loop in Ise Bay using and ecosystem model. J. Japan Soc. Civ. Eng. Ser. B2 (Coastal Eng. 71, 1411-1416) (In Japanese).

Officer, C.B., Biggs, R.B., Taft, J.L., Cronin, L.E., Tyler, M.A., Boynton, W.R., 1984. Chesapeake Bay anoxia: Origin, development, and significance. Science (80-.). 223, 22–27. doi:https://doi.org/10.1126/science.223.4631.22.

Padiyedath Gopalan, S., Kawamura, A., Takasaki, T., Amaguchi, H., Azhikodan, G., 2018. An effective storage function model for an urban watershed in terms of hydrograph reproducibility and Akaike information criterion. J. Hydrol. 563, 657–668. https://doi.org/10.1016/j.jhydrol.2018.06.035.

Parasad, R., 1967. A nonlinear hydrologic system response model. J. Hydraul. Div. 93, 201–222.

Rabalais, N.N., Turner, R.E., Wiseman, W.J., 2002. Gulf of Mexico hypoxia, a.k.a. "The dead zone.". Annu. Rev. Ecol. Syst. 33, 235–263. https://doi.org/10.1146/annurev.ecolsys.33.010802.150513.

Rana, F.M., Adamo, M., Lucas, R., Blonda, P., 2019. Sea surface wind retrieval in coastal areas by means of Sentinel-1 and numerical weather prediction model data. Remote Sens. Environ. 225, 379–391. https://doi.org/10.1016/j.rse.2019.03.019.

Rheuban, J.E., Doney, S.C., Cooley, S.R., Hart, D.R., 2018. Projected impacts of future climate change, ocean acidification, and management on the US Atlantic sea scallop (Placopecten magellanicus) fishery. PLoS One 13, 1–21. https://doi.org/10.1371/journal.pone.0203536.

Sashiyama, S., Yamamoto, K., 2014. Method for Evaluating the Influence of Obstruction of Sea Breeze by Clusters of High-Rise Buildings on the Urban Heat Island Effect. J. Environ. Prot. (Irvine,. Calif). 05, 983–996. doi:https://doi.org/10.4236/jep.2014.511099.

Shchepetkin, A.F., McWilliams, J.C., 2005. The regional oceanic modeling system (ROMS): a split-explicit, free-surface, topography-following-coordinate oceanic model. Ocean Model 9, 347–404. https://doi.org/10.1016/j.ocemod.2004.08.002.

Shimadera, H., Kojima, T., Kondo, A., Inoue, Y., 2015a. Performance comparison of CMAQ and CAMx for one-year PM 2.5 simulation in Japan. Environ. Pollut. 57, 146–161.

Shimadera, H., Kondo, A., Shrestha, K.L., Kitaoka, K., Inoue, Y., 2015b. Numerical evaluation of the impact of urbanization on summertime precipitation in Osaka. Japan. Adv. Meteorol. 2015. https://doi.org/10.1155/2015/379361.

Skamarock, W.C., Klemp, J.B., Dudhia, J., Gill, D.O., Zhiquan, L., Berner, J., Wang, W., Powers, J.G., Duda, M.G., Barker, D.M., Huang, X.-Y., 2019. A Description of the Advanced Research WRF Model Version 4. NCAR Tech. Note NCAR/TN-475+STR 145. doi: https://doi.org/10.5065/1dfh-6p97.

Smagorinksy, J., 1963. General circulation experiments with primitive equations. Mon. Weather Rev. 91.

Song, G., Zhao, L., Chai, F., Liu, F., Li, M., 2020. Summertime oxygen depletion and acidification in Bohai Sea. China 7, 1–11. https://doi.org/10.3389/fmars.2020.00252.

Stramma, L., Johnson, G.C., Sprintall, J., Mohrholz, V., 2008. Expanding oxygen-minimum zones in the tropical oceans. Science (80-.). 320, 655–658. doi:https://doi.org/10.1126/science.1153847.

Sugahara, I., Kimura, T., Hayashi, K., 1988. Distribution and Generic Composition of Denitrifying Bacteria in Coastal and Oceanic Bottom Sediments. Nippon Suisan Gakkaishi (Japanese Ed. 54, 1005–1010. doi:https://doi.org/10.2331/suisan.54.1005.

Suzuki, C., 2016. Assessing change of environmental dynamics by legislation in Japan, using red tide occurrence in Ise Bay as an indicator. Mar. Pollut. Bull. 102, 283–288. https://doi.org/10.1016/j.marpolbul.2015.08.010.

Tanaka, Y., Ikeda, K., 2015. Analyse of relationship between hypoxia and age in Ise Bay by using numerical simulation. J. Japan Soc. Civ. Eng. Ser. B2 (Coastal Eng. 71, I_1261-I_1266. doi:https://doi.org/10.2208/kaigan.71.I_1261 (In Japanese).

Tanaka, Y., Suzuki, K., 2010. Development of Non-Hydrostatic Numerical Model for Stratified Flow and Upwelling in Estuary and Coastal Areas. Report: Port and Airport Research Institute 49(1), (3-25) (In Japanese).

Tanaka, Y., Nakamura, Y., Suzuki, K., Inoue, T., Nishimura, Y., 2011a. Development on the Pelagic Ecosystem Model Considering the Microbial Loop for Estuary and Coastal Areas Report: Port and Airport Research Institute 50(2), (3–68) (In Japanese).

Tanaka, Y., Nakamura, Y., Suzuki, K., Inoue, T., Nishimura, Y., Uchida, Y., Shirasaki, M., 2011b. Development of a Pelagic Ecosystem Model Considering the Microbial Loop and Field Evaluation in Ise Bay. J. Japan Soc. Civ. Eng. Ser. B2 (Coastal Eng. 67, I_1041-I_1045. doi:https://doi.org/10.2208/kaigan.67.i_1041 (In Japanese).

Tanaka, Y., Kanno, A., Shinohara, R., 2014. Effects of global brightening on primary production and hypoxia in Ise Bay. Japan. Estuar. Coast. Shelf Sci. 148, 97–108. https://doi.org/10.1016/j.ecss.2014.06.010.

Tang, J., Niu, X., Wang, S., Gao, H., Wang, X., Wu, J., 2016. Statistical downscaling and dynamical downscaling of regional climate in China: present climate evaluations and future climate projections. J. Geophys. Res. Atmos. 121, 2110–2129. https://doi.org/10.1002/2015JD023977.

Thompson, G., Rasmussen, R.M., Manning, K., 2004. Explicit forecasts of winter precipitation using an improved bulk microphysics scheme. Part I: Description and Sensitivity Analysis. Mon. Weather Rev. 132, 519–542.

USEPA, 2003. Ambient Water Quality Criteria for Dissolved Oxygen. Water Clarity and Chlorophyll, Science And Technology.

Vaquer-Sunyer, R., Duarte, C.M., 2008. Thresholds of hypoxia for marine biodiversity. Proc. Natl. Acad. Sci. U. S. A. 105, 15452–15457. https://doi.org/10.1073/pnas.0803833105.

Warren, I.R., Bach, H.K., 1992. MIKE 21: a modelling system for estuaries, coastal waters and seas. Environ. Softw. 7, 229–240. https://doi.org/10.1016/0266-9838(92)90006-P.

Westrich, J.T., Berner, R.A., 1984. The role of sedimentary organic matter in bacterial sulfate reduction: the G model tested. Limnol. Oceanogr. 29, 236–249. https://doi.org/10.4319/lo.1984.29.2.0236.

Yamamoto, S., Nakamura, Y., Tanaka, Y., Suzuki, T., 2015. Analysis of blue tide events in Tokyo bay using 3-D ecosystem model with sulfur oxidization. J. Japan Soc. Civ. Eng. Ser. B2 (Coastal Eng. 71, 1279-1284) (In Japanese).

Yelland, M.J., Moat, B.I., Taylor, P.K., Pascal, R.W., Hutchings, J., Cornell, V.C., 1998. Wind stress measurements from the open ocean corrected for airflow distortion by the ship. J. Phys. Oceanogr. 28, 1511–1526. https://doi.org/10.1175/1520-0485(1998)028<1511:WSMFTO>2.0.CO;2.